Bright-field transmission imaging of carbon nanofibers on bulk substrate using conventional scanning electron microscopy

Makoto Suzuki,[a] Quoc Ngo, Hirohiko Kitsuki, Kristofer Gleason, Yusuke Ominami, and Cary Y. Yang
Center for Nanostructures, Santa Clara University, Santa Clara, California 95053

Toshishige Yamada,[b] Alan M. Cassell, and Jun Li
NASA Ames Research Center, Moffett Field, California 94035

(Received 10 April 2007; accepted 31 July 2007; published 30 August 2007)

The authors present scanning transmission electron microscopy (STEM) of carbon nanofibers (CNFs) on a bulk substrate using conventional scanning electron microscopy (SEM) without specimen thinning. By utilizing the electron beam tilted >85° from the substrate normal, bright-field STEM contrast is obtained for the CNFs on substrate with conventional SEM. Analysis of the observed contrast using Monte Carlo simulation shows that the weakly scattered electrons transmitted from the CNF are selectively enhanced by the largely tilted substrate and result in the observed STEM contrast. This mechanism provides a useful STEM imaging technique to investigate the internal structure of materials on bulk substrates without destructive specimen thinning. © *2007 American Vacuum Society.* [DOI: 10.1116/1.2775457]

I. INTRODUCTION

Progress in nanoscale science has been accompanied by advances in precise imaging techniques. High-resolution imaging methods such as scanning electron microscopy (SEM), transmission electron microscopy (TEM), and scanning transmission electron microscopy (STEM) have provided direct evidence of nanoscale phenomena using recently developed *in situ* imaging techniques.[1–5] While SEM is applicable to a wide range of sample geometry and mainly provides surface information, internal structural analysis with high spatial resolution using TEM and STEM requires an electron transparent sample with a thickness of less than several hundred nanometers.[6] Some of the nanoscale devices, however, are fabricated on a thick substrate (>100 μm) which does not allow the electron beam to penetrate the device. One such structure is carbon nanotube (CNT) field-effect transistors[7,8] fabricated on a semiconductor substrate with patterned electrodes, which makes it difficult to investigate the internal structure of CNTs without thinning the sample. To overcome this difficulty, several TEM (or STEM) compatible device structures have been proposed, including the CNT device structure fabricated on a silicon nitride membrane[2,9–11] and the device structure fabricated on the thick Si substrate with an etched groove underneath the CNTs.[12] Although these techniques are quite useful to study the intrinsic property of nanotubes, recent studies[13–15] indicate that heat dissipation via the substrate plays an important role in their electrical characteristics. Thus, it is essential to take into account the heat dissipated from the current-carrying device into the underlying thick substrate. Although cleaving and etching techniques of the Si substrate after electrical measurements have been proposed for detailed TEM imaging,[16] they are not suitable for simultaneous imaging and electrical measurement or for reliability study of structural changes before, after, and during high-current stress. From a large-scale integration perspective, the large sample capability (>10 mm), which is realized in conventional SEM, is an important consideration.

In Fig. 1, several geometries of STEM imaging are shown. In conventional TEM or dedicated STEM imaging[17] [Fig. 1(a)], samples are supported on an electron transparent support film and transmitted electrons are captured by the detector placed below after passing the postspecimen optics to select the signals and contrast modes (i.e., bright-field, dark-field, or diffraction signal). A simple realization[18,19] of STEM imaging in conventional SEM is illustrated in Fig. 1(b). By placing an electron detector directly below the sample in the specimen chamber, the transmission signal can be obtained. A simplified configuration[20] [Fig. 1(c)] for STEM imaging is realized by introducing a highly reflective metal block below the sample instead of an additional detector below the sample. It converts transmitted electrons to secondary electrons (SEs) to be captured by the side-mounted Everhart-Thornley (ET) detector of SEM. This configuration provides an inexpensive solution for STEM imaging using conventional SEM since this does not require any additional electronics. Although these STEM signal detection techniques with conventional SEM relax the instrumental requirement, they do not ease sample preparation and still require sample thinning and the electron transparent support film below the sample.

In this article, we demonstrate a STEM imaging technique using conventional SEM without sample thinning. We extend the technique shown in Fig. 1(c) to samples on a substrate, as shown in Fig. 1(d). Here, the substrate serves as a highly reflective material to convert incident electrons to SEs. By using a grazing incident electron beam tilted >85° from the

[a]Present address: Hitachi High Technologies, Corp., Hitachinaka, Ibaraki 312-8504, Japan; electronic mail: suzuki-makoto@naka.hitachi-hitec.com
[b]Also at Center for Nanostructures, Santa Clara University.

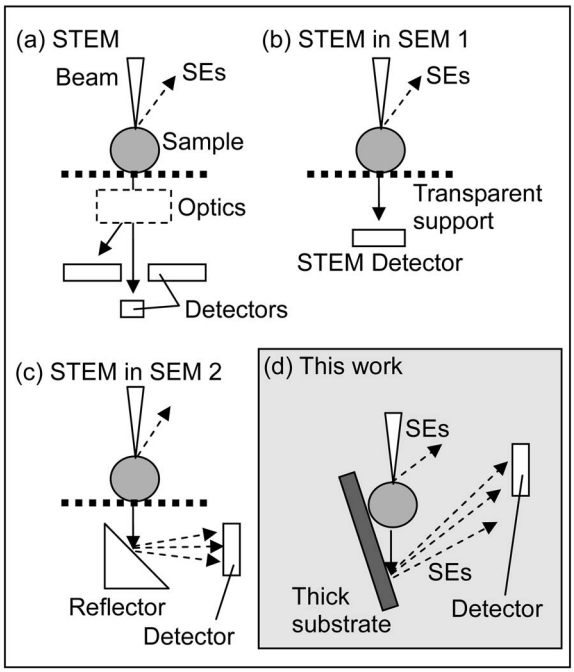

FIG. 1. Several STEM imaging techniques. (a) Dedicated STEM with postspecimen optics. It contains two or three detectors, which can be selected in conjunction with operation of the optics. (b) A simple realization of STEM imaging in a conventional SEM. A STEM detector is placed directly below the sample. (c) A more simplified method for STEM. A high SE emission material is placed below the sample and the produced SEs are captured by an ET detector. (d) Proposed technique for STEM imaging of the sample on a thick substrate.

substrate normal, we observe bright-field STEM contrast with a through-the-lens (TTL) detector placed above the sample and objective lens. The contrast mechanism is analyzed using Monte Carlo simulation, showing that the highly tilted substrate is primarily responsible for bright-field STEM contrast since the substrate effectively converts only weakly scattered electrons by the carbon nanofiber (CNF) into SEs. It is also shown that the strong SE signal enhancement using the tilted substrate overwhelms the SE signal from the CNF, both of which cannot be separated even by using additional optics because both signals come from close proximity unlike the method shown in Fig. 1(c), resulting in clear bright-field STEM contrast. While similar imaging techniques using weakly deflected forward scattered electrons (low-loss electrons) from the largely tilted specimen have been proposed,[21,22] these are high-resolution surface imaging techniques resulting from the smaller spatial spread of low-loss electrons inside the specimen,[23] and are not relevant to transmission imaging, as presented in this work.

II. EXPERIMENT

The specimen used here is a CNF (Refs. 24–26) grown by plasma-enhanced chemical vapor deposition[27,28] with a Ni catalyst layer on Si substrate. A 30-nm-thick Ti adhesion layer was used between 35-nm-thick Ni layer and Si. A gas mixture of $NH_3:C_2H_2(4:1)$ was introduced for the reaction and kept at 4 Torr. Details of the reaction conditions are

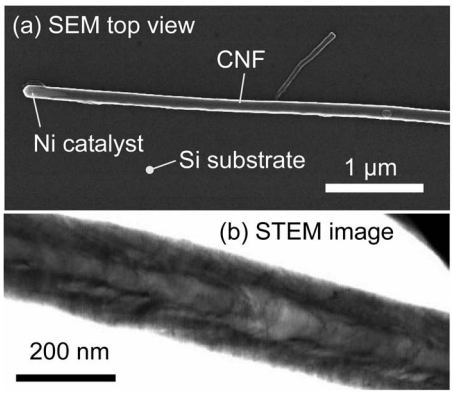

FIG. 2. (a) SEM image of a CNF on Si substrate. The incident beam is perpendicular to the substrate. A bright portion at the left end of the CNF indicates a Ni catalyst particle. (b) Bright-field STEM image of a CNF captured using the method shown in Fig. 1(b).

described elsewhere.[29] As-grown CNFs are carefully removed from the growth substrate and prepared on another polished flat Si substrate (~500 μm thick) for nanofiber devices. The typical diameter and length of CNFs are 200 nm and 10 μm, respectively.

The SEM used for this study is a Hitachi S-4800 field-emission SEM with an accelerating voltage of 30 kV and a probe diameter of 1 nm. Signal detectors are placed above the objective lens for efficient SE collection (TTL detector) and at the side of the specimen chamber (ET detector). The efficient SE collection system[30] using the TTL detector and a snorkel-type objective lens coupled with a signal selection filter and extraction electric field near the specimen enables one to collect the SEs irrespective of the SE emitting direction and their energy spread. The images presented below are captured with the TTL detector; thus the image contrast is formed mainly by SEs emitted from the specimen with kinetic energies below 50 eV. A 30 keV electron beam is used, the probe current is 40 pA, and the working distance is typically 8 mm.

III. RESULTS

The SEM image of a CNF resting on the Si substrate is shown in Fig. 2(a). The 30 keV electron beam is irradiated perpendicularly to the substrate. The contrast of the CNF is mainly formed by SEs from the CNF surface, and thus the topological contrast of the surface of the CNF with enhanced edge brightness is obtained, as reported previously.[31] A Ni catalyst particle is seen at the left end, providing a bright contrast due to enhanced SE emission by a larger backscattering coefficient of Ni than carbon.[32] The internal density profile of another CNF is also shown in Fig. 2(b), obtained by using an electron transparent support film and additional STEM detector below the sample, as illustrated in Fig. 1(b). Since the detector captures the transmitted electrons including the on-axis (unscattered) signal, it provides bright-field STEM contrast. The internal structure exhibits the cup-shaped morphology of graphite layers. This is consistent with previously studied high-resolution STEM

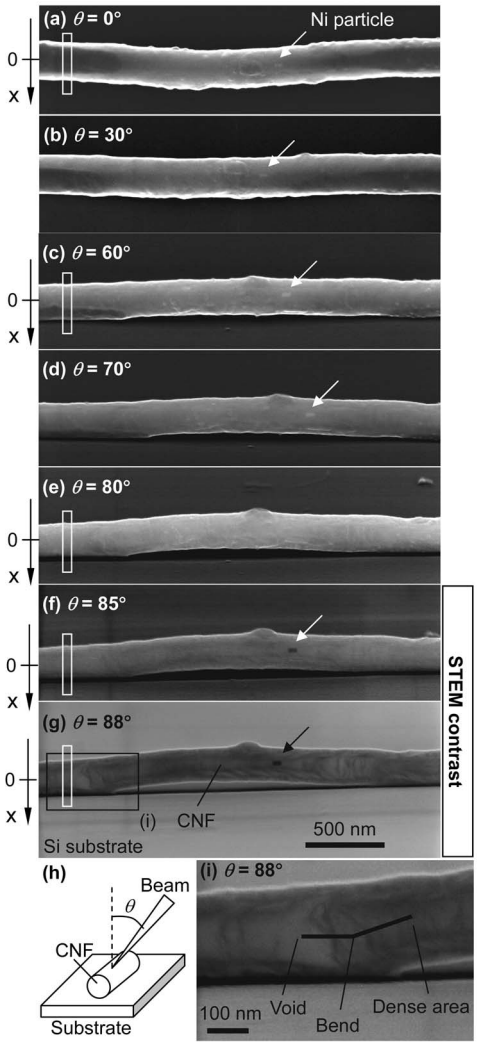

FIG. 3. [(a)–(g)] Tilt angle dependence of SEM images of a CNF on Si substrate. A small Ni particle is indicated by an arrow. Bright-field STEM contrast is observed at $\theta \geqslant 85°$. Elongated white boxes and x axes correspond to the positions and directions of the line profiles, respectively, shown in Figs. 4(c)–4(g). (h) Schematic of the sample and electron beam configuration. (i) Detailed internal morphology of the CNF shown in (g).

imaging,[33] providing a reference structure for the present STEM imaging technique on a thick substrate, as described below.

The tilt angle dependence of the SEM images of a CNF on Si substrate is illustrated in Figs. 3(a)–3(g). The tilt angle (θ) is defined as the angle of the beam measured from the substrate normal, as shown in Fig. 3(h), and the plane of the beam tilt is perpendicular to the CNF axis. At moderate tilt angles of $\theta \leqslant 70°$ [Figs. 3(a)–3(d)], the surface morphology of the CNF can be seen, exhibiting a typical SE contrast of SEM, as shown in Fig. 2(a). Also, a small Ni catalyst particle embedded in the CNF is visible as a bright spot, as indicated by arrows. At $\theta = 80°$, this bright Ni particle disappears [Fig. 3(e)], and as θ increases over 85°, the surface detail of the CNF also disappears but the internal density profile becomes visible [Figs. 3(f), 3(g), and 3(i)] just like the STEM image shown in Fig. 2(b). The dense graphite part in the CNF appears darker than other low-density regions, and thus revealing the bright-field STEM contrast. Also, the embedded Ni particle becomes darker, and it shows that the observed contrast correlates with the transmission probability of the electron beam as expected in bright-field STEM contrast. This result is nontrivial because as long as $\theta < 90°$, the substrate impedes the electrons transmitted through the CNF; thus a STEM image cannot be obtained even with the STEM detector below the sample, as shown in Fig. 1(b). It should also be noted that it is not useful to use the beam parallel to the substrate ($\theta = 90°$) to detect the transmitted electrons using the STEM detector, as in Fig. 1(b). This is because both the incident and transmitted electrons are interrupted by other CNFs placed in front of or behind the nanofiber of interest, thus making transmission imaging difficult. Using this technique, we can study the density profile of the graphitic layers comprising the CNF, which is essential to understand the electron transport through the CNF. As shown in Fig. 3(g), the internal density profile of the CNF is not uniform along the fiber axis. We can correlate the internal structure of the CNF and its relative configuration with the underlying substrate. As shown in Fig. 3(g), the midsection of the CNF is not in contact with the substrate. This is also confirmed by the observed bright contrast coming from the detached part of the CNF in Fig. 3(a), caused by the SE signal from the underlying substrate, as discussed in Ref. 30. A STEM image shown in Fig. 3(i) exhibits a bend caused by the internal structural nonuniformity, where a void exists adjacent to a dense graphite region.

IV. ANALYSIS AND DISCUSSION

To analyze the obtained bright-field STEM contrast, we employ a Monte Carlo simulation of the SEM image formation.[34] In the Monte Carlo procedure, trajectories of incident electrons are traced with successive elastic scatterings with a Mott elastic cross section[35] and continuous energy loss due to inelastic processes.[36,37] We use the semiempirical SE generation model,[38,39] where the number of the SEs generated is proportional to the amount of energy loss of the incident beam, and the number of the emitted SEs decreases along the escape path from the generation point to the material surface. Although simplified for analytic calculation,[39] the model can provide a more accurate description when employed in the Monte Carlo modeling with the model parameters such as the SE generation energy and the SE mean free path carefully chosen to reproduce the experimentally observed SE emission coefficient.[34] The choice of these parameters for the CNF and the Si substrate is discussed in detail in our previous study.[40] We assume that the angular distribution of SE generation is isotropic (there is no preferred SE propagation direction) and the SE emission from the surface obeys the cosine distribution accordingly,[38] $dn_{\mathrm{SE}} \sim d(\cos\phi) = -\sin\phi d\phi$, where ϕ is defined as the transverse angle of the SE emission measured from the surface normal. We also assume that this distribution is independent of the tilt angle (θ) of the incident beam,[38] except for its magnitude which increases monotonically with θ.[32,38] This

must be valid even at a very large tilt angle of 88° because the SE generation anisotropy, if any, will not have any correlation with the surface position of the material. This means that the SE propagation will be independent of the incident beam direction,[41] and we use the cosine distribution for all the emitting SEs from the material surface. As for the signal detection, we count the number of captured SEs in obtaining the signal profile. We approximate the SE trajectory outside the specimen as a straight line and assume that all the emitted SEs are captured by the detector successfully except for the SEs that collide with the CNF or substrate. While the SE detection system we used in the experiment has a wide SE acceptance window,[30] our treatment of all the SE capturing in the simulation could be an oversimplification. In fact, the specimen is placed in a magnetic field of the objective lens that can bend the SE trajectory and reduce the capturing probability. Our scope is, however, to provide a clear physical mechanism for why different images are obtained with an increasing tilt angle θ, as shown in Fig. 3, and the assumption of perfect SE collection efficiency will not change any of the essential features there. It is shown below that our model matches the experimental findings quite well.

The sample geometry is defined as a hollow carbon fiber on the flat Si substrate, as shown in Fig. 4(a). The thickness of the Si substrate is set at 500 μm. Here, the CNF outer diameter and the inner hollow diameter are assumed to be 200 and 100 nm, respectively. By using the hollow structure, the signal profile can be easily interpreted, i.e., the center hollow would appear brighter using bright-field STEM.

In Figs. 4(c)–4(g), the observed line profiles extracted from Fig. 3 with different tilt angles θ are shown. The corresponding line positions are surrounded by the elongated white boxes in Figs. 3(a), 3(c), and 3(e)–3(g). The x axis for each profile is also defined at the left end of each figure. The bright-field STEM contrast observed at $\theta=88°$ [Fig. 3(g)] corresponds to a small hump observed at $-50\ \text{nm}<x<50\ \text{nm}$ in Fig. 4(g), where the void region provides higher SE intensity.

In Figs. 4(h)–4(l), the calculated total SE profiles with different tilt angles θ are shown with solid lines. Each data point is obtained by computing 5000 incident electron trajectories using Monte Carlo simulation. The tilt angle θ is defined as the angle of the electron beam measured from the substrate normal, as shown in Fig. 4(a). The line scan is performed along the x axis, which is illustrated in Figs. 4(a) and 4(b). The origin is set at the center of the CNF and the positive direction is the arrow direction in Figs. 4(a) and 4(b). Thus the CNF lies between $x=-100$ nm and $x=100$ nm, and the hollow core between $x=-50$ nm and $x=50$ nm. The overall trend of these profiles matches well the experimental data shown in Figs. 4(c)–4(g). As can be seen in the figure, the SE profiles do not exhibit an internal hollow structure when $\theta<85°$. At $\theta\geqslant 85°$, however, the SE profile shows a clear hump corresponding to the inner hollow structure (at the position between −50 and 50 nm). This means that the bright-field STEM contrast is obtained with a largely tilted beam, consistent with Fig. 4(g). As a reference, the SE profiles of a CNF with no inner hollow region (solid CNF) and the same outer diameter, as schematically illustrated in Fig. 4(b), are shown with broken lines in Figs. 4(h)–4(l). While the difference between these two structures in SE profile is negligible at θ smaller than 80°, the two profiles exhibit a significant difference in the positions between −50 and 50 nm at $\theta\geqslant 85°$, showing that the internal structure is imaged only when $\theta\geqslant 85°$ and that the existence of the inner hollow does contribute to the increase of the detected signal at this angle. Thus, a crossover of the origin of the SE signal should take place at around $\theta=85°$, which confirms our experimental observation shown in Fig. 3. The excellent match between the calculation and experimental results supports our assumption for the calculation of the SE generation and detection as described above.

While the calculated profiles coincide with the experimental ones, one of the great advantages of the Monte Carlo modeling is that we can trace the SE emission point of each captured SE. In order to explore the origin of this image contrast, we separately count the SE signals from the CNF and the Si substrate. Since each SE has its generation point along the incident electron path and also its emission point on the specimen surface, we can differentiate between the SE signal originating from the CNF and that from the substrate. The SE signal profiles from the hollow CNF for various θ's are shown in Figs. 4(m)–4(q) and those from Si substrate in Figs. 4(r)–4(v) with solid lines. The sum of these two profiles leads to the total SE profile shown in Figs. 4(h)–4(l). Each data point is again obtained with 5000 incident electrons. Also, the SE profiles obtained by using the solid CNF are shown with broken lines. As shown in Figs. 4(n)–4(q), the SE signal profile from the CNF does not change significantly with θ. On the other hand, the SE profile from the substrate [Figs. 4(s)–4(v)] changes substantially with increasing θ. It can be seen that the average SE signal intensity from the substrate increases with increasing θ, while that from the CNF is independent of θ. This is due to the conventional surface tilt effect of SE signal,[32,38] and thus the SE profile from the substrate dominates the total SE profile at large θ. Note that the vertical scales are all different in Figs. 4(r)–4(v). At $\theta\leqslant 80°$, profiles show a sharp dip as indicated by "A" in the figures. The position of the dip corresponds to the position where the SE emission is suppressed by the CNF above it. At $\theta\geqslant 85°$, besides the sharp dip, another broad dip appears, indicated by "B," at the position where the substrate is masked by the CNF (from −100 to +100 nm). Inside this broad dip, the hollow CNF provides the SE signal increase corresponding to the hollow region, which provides the bright-field STEM contrast. By comparing Figs. 4(l) and 4(v), it can be seen that the bright-field STEM contrast mostly results from the broad dip appearing in the SE profile from the substrate. We will now explore the origin of this broad dip as follows.

There are two possible reasons for this broad dip. One is the decrease of the number of incident electrons into the substrate due to backscattering from the CNF. The other mechanism also involves the decrease in the incident elec-

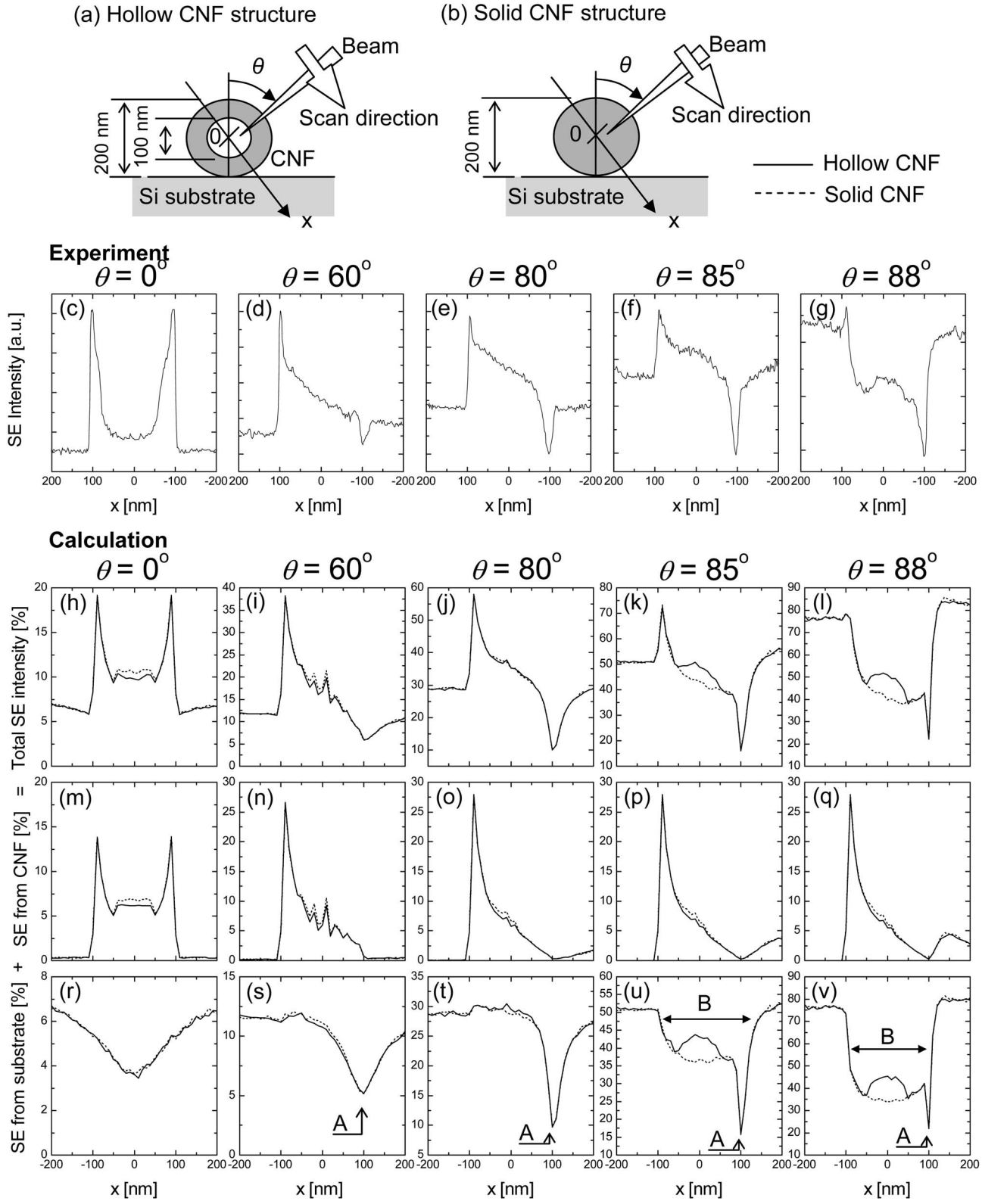

FIG. 4. (a) Schematic of hollow CNF on Si substrate. (b) Schematic of solid CNF on Si substrate. The x axis in the line profile (a black arrow) and the line scan direction of the electron beam (a white arrow) are both defined in (a) and (b). [(c)–(g)] Experimental line profiles of the CNF extracted from Fig. 3. [(h)–(v)] Monte Carlo simulations of the SE profiles of a hollow CNF on Si substrate (solid lines) and of a solid CNF on Si substrate (broken lines). The outer diameter is 200 nm for both types of CNFs, and inner diameter of the hollow CNF is 100 nm. In (h)–(l), total SE profiles are shown for various tilt angles θ. (m)–(q) show SE profiles from the CNF, and (r)–(v) represent those from the Si substrate. 5000 incident electrons are used in the Monte Carlo simulation to obtain each data point.

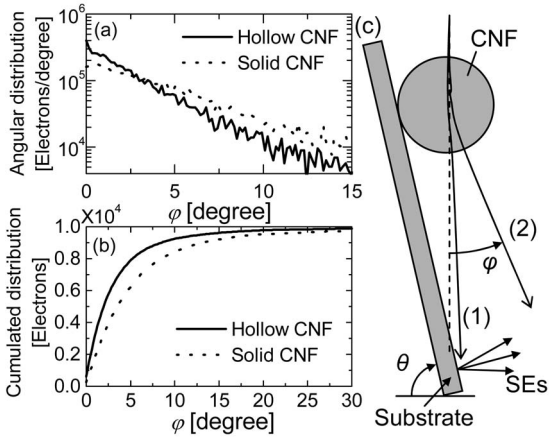

FIG. 5. (a) Angular distribution of the 30 keV incident electrons after passing through the CNF with the diameter of 200 nm. 10 000 incident electrons are used in each Monte Carlo simulation. Solid lines represent the hollow CNF, and broken lines represent the solid CNF. (b) Cumulated distribution of the 30 keV incident electrons. (c) Schematic of electron spread due to the CNF. Weakly deflected electrons (1) collide with the substrate to produce SEs, while the largely deflected electrons (2) have a trajectory away from the substrate.

trons, but is due to forward scattering of electrons caused by the CNF. The absence of a broad dip at $\theta \leqslant 80°$ excludes the first mechanism, since the backscattering probability from the cylindrical CNF should be independent of θ. To examine the second mechanism in our study, we again employ Monte Carlo simulation to calculate the angular distribution of the incident electrons after passing through the CNF with and without the hollow core. The result is shown in Fig. 5(a). Here, the distribution is calculated using 10 000 incident electrons. The angle φ is defined as the angle of the deflected incident electron beam, as shown schematically in Fig. 5(c). Solid and broken lines represent the data for the hollow and solid CNFs, respectively. The figure clearly shows that the hollow CNF provides a sharper distribution, indicating a smaller scattering probability. Indeed, the root-mean-square deflection angles (φ_{rms}) are calculated as 5.3° and 7.2° for the hollow and solid CNFs, respectively. By integrating this distribution with respect to φ, we obtain the cumulated number of electrons inside the half angle φ of the beam spread. The result is plotted in Fig. 5(b). Again, solid and broken lines represent the data for the hollow and solid CNFs, respectively. As can be seen, while both curves converge to the total number of incident electrons of 10 000 at large φ, they drop sharply at small φ. Thus, only a small fraction of the total electrons are inside the cone with a half angle of φ and other electrons are scattered outside the cone. When the tilted beam with the angle of $\theta = 90° - \varphi$ from the substrate normal is used, only those electrons which are weakly scattered into the cone with half angle φ can reach the substrate [indicated as (1) in Fig. 5(c)] to produce SEs, and half of the scattered electrons outside the cone travel away from the substrate [indicated as (2) in Fig. 5(c)]. These heavily scattered electrons by the CNF do not contribute to SE signal from the substrate, leading to the broad dip B in Figs. 4(u) and 4(v). The threshold value of θ for the STEM contrast (85°) is consistent with the root-mean-square scattering angle of $\varphi_{rms} = 5.2°$. Another important feature is a significant difference between these two curves in Fig. 5(b) at small φ. Since the number of electrons inside the small cone with a half angle of φ is larger for the hollow CNF than the solid CNF and the difference becomes more than 10% for $\varphi < 5°$, the number of electrons that reach the substrate is highly sensitive to the internal density of the CNF. From this analysis, we conclude that the broad dip comes from the forward scattering deflection by the CNF and that the largely tilted beam is essential for bright-field STEM contrast, because (i) tilting the beam increases the SE signal from the substrate and (ii) the SE signal from the substrate correlates with the variation of the angular spread of the incident electrons, which in turn depends on the internal density profile of the CNF.

Finally, we should also discuss the contrast reversal of the small Ni particle observed in Fig. 3. Disappearance of the Ni particle at $\theta = 80°$ [Fig. 3(e)] shows that the larger SE emission of Ni observed at smaller θ cancels out the dark contrast from the substrate. At larger θ, the latter effect becomes dominant; thus bright-field contrast of the Ni particle can be seen. The particle is very small (30 nm) compared to the CNF diameter (200 nm), suggesting that the threshold θ of the bright-field STEM contrast for this Ni particle is about 80°, smaller than that of the CNF (~85°). Actually, the root-mean-square deflection angle (φ_{rms}) for the Ni particle with a diameter of 30 nm is calculated as 9.1°, in the same way as described above. Thus, the threshold of the bright-field STEM contrast should be around $\theta = 90° - 9.1° \sim 81°$, consistent with the experimental observation.

V. CONCLUSION

A transmission imaging technique using conventional SEM for carbon nanofiber on Si substrate has been presented. Based on the analysis of the contrast mechanism using Monte Carlo simulation, the SE signal enhancement from a highly tilted substrate and its sensitivity to beam spreading by the CNF reveal the internal density profile of the CNF. This mechanism is equivalent to bright-field STEM contrast. This technique provides a very useful STEM imaging method using conventional SEM for the sample on a bulk substrate without the use of any destructive sample-thinning process.

ACKNOWLEDGMENTS

The authors are grateful to Bill Roth and Mark Betts of Hitachi High-Technologies America, Inc., and Patrick Wilhite for their technical support. They are also indebted to Xiao Feng Zhang, Yuji Awano, and Yasuko Aoki for valuable comments and suggestions.

[1] J. Y. Huang, S. Chen, S. H. Jo, Z. Wang, D. X. Han, G. Chen, M. S. Dresselhaus, and Z. F. Ren, Phys. Rev. Lett. **94**, 236802 (2005).
[2] T. D. Yuzvinsky *et al.*, Appl. Phys. Lett. **87**, 083103 (2005).
[3] J. Y. Huang *et al.*, Nature (London) **439**, 281 (2006).
[4] S. Jesse, M. A. Guillorn, I. N. Ivanov, A. A. Puretzky, J. Y. Howe, P. F. Britt, and D. B. Geohegan, Appl. Phys. Lett. **89**, 013114 (2006).
[5] R. Sharma and Z. Iqbal, Appl. Phys. Lett. **84**, 990 (2004).

[6]A. V. Crewe and T. Groves, J. Appl. Phys. **45**, 3662 (1974).
[7]S. J. Tans, A. R. M. Verschueren, and C. Dekker, Nature (London) **393**, 49 (1998).
[8]R. Martel, T. Schmidt, H. R. Shea, T. Hertel, and Ph. Avouris, Appl. Phys. Lett. **73**, 2447 (1998).
[9]A. Y. Kasumov, I. I. Khodos, P. M. Ajayan, and C. Colliex, Europhys. Lett. **34**, 429 (1996).
[10]A. Kis *et al.*, Nat. Mater. **3**, 153 (2004).
[11]S. B. Chikkannanavar, D. E. Luzzi, S. Paulson, and A. T. Johnson, Jr., Nano Lett. **5**, 151 (2005).
[12]T. Kim, J.-M. Zuo, E. A. Olson, and I. Petrov, Appl. Phys. Lett. **87**, 173108 (2005).
[13]E. Pop, D. Mann, J. Cao, Q. Wang, K. Goodson, and H. Dai, Phys. Rev. Lett. **95**, 155505 (2005).
[14]M. A. Kuroda, A. Cangellaris, and J. P. Leburton, Phys. Rev. Lett. **95**, 266803 (2005).
[15]M. Lazzeri, S. Piscanec, F. Mauri, A. C. Ferrari, and J. Robertson, Phys. Rev. Lett. **95**, 236802 (2005).
[16]J. C. Meyer, D. Obergfell, S. Roth, S. Yang, and S. Yang, Appl. Phys. Lett. **85**, 2911 (2004).
[17]B. Fultz and J. M. Howe, *Transmission Electron Microscopy and Diffractometry of Materials*, 2nd ed. (Springer, Berlin, 2005), Chap. 2, pp. 63–104.
[18]R. J. Woolf, D. C. Joy, and D. W. Tansley, J. Phys. E **5**, 230 (1972).
[19]U. Golla, B. Schindler, and L. Reimer, J. Microsc. **173**, 219 (1994).
[20]B. J. Crawford and C. R. W. Liley, J. Phys. E **3**, 461 (1970).
[21]O. C. Wells, Appl. Phys. Lett. **16**, 151 (1970); **19**, 232 (1971).
[22]O. C. Wells and P. C. Cheng, J. Appl. Phys. **62**, 4872 (1987).
[23]W. E. Vanderlinde, 29th International Symposium for Testing and Failure Analysis, Santa Clara, CA, 2003 (unpublished), pp. 158–165.
[24]S. Helveg, C. López-Cartes, J. Sehested, P. L. Hansen, B. S. Clausen, J. R. Rostrup-Nielsen, F. Abild-Pedersen, and J. K. Nørskov, Nature (London) **427**, 426 (2004).
[25]A. V. Melechko, V. I. Merkulov, T. E. McKnight, M. A. Guillorn, K. L. Klein, D. H. Lowndes, and M. L. Simpson, J. Appl. Phys. **97**, 041301 (2005).
[26]Q. Ngo, A. M. Cassell, A. J. Austin, J. Li, S. Krishnan, M. Meyyappan, and C. Y. Yang, IEEE Electron Device Lett. **27**, 221 (2006).
[27]Y. Chen, Z. L. Wang, J. S. Yin, D. J. Johnson, and R. H. Prince, Chem. Phys. Lett. **272**, 178 (1997).
[28]Z. F. Ren, Z. P. Huang, J. W. Xu, J. H. Wang, P. Bush, M. P. Siegal, and P. N. Provencio, Science **282**, 1105 (1998).
[29]B. A. Cruden, A. M. Cassell, Q. Ye, and M. Meyyappan, J. Appl. Phys. **94**, 4070 (2003).
[30]S. Takeuchi, A. Muto, M. Nakagawa, S. White, R. Tamochi, M. Sato, M. Yamada, and D. C. Joy, Microsc. Microanal. **10**, 950 (2004).
[31]M. Suzuki, Y. Ominami, Q. Ngo, C. Y. Yang, T. Yamada, A. M. Cassell, and J. Li, J. Appl. Phys. **100**, 104305 (2006).
[32]H. Seiler, J. Appl. Phys. **54**, R1 (1983).
[33]Y. Ominami *et al.*, Appl. Phys. Lett. **87**, 233105 (2005).
[34]D. C. Joy, *Monte Carlo Modeling for Electron Microscopy and Microanalysis* (Oxford, New York, 1995), Chap. 8, pp. 134–173.
[35]Z. Czyżewski, D. O. MacCallum, A. Roming, and D. C. Joy, J. Appl. Phys. **68**, 3066 (1990).
[36]H. Bethe, Ann. Phys. **5**, 325 (1930).
[37]D. C. Joy and S. Luo, Scanning **11**, 176 (1989).
[38]K. Kanaya and H. Kawakatsu, J. Phys. D **5**, 1727 (1972).
[39]J. Schou, Scanning Microsc. **2**, 607 (1988).
[40]M. Suzuki, T. Yamada, and C. Y. Yang, Appl. Phys. Lett. **90**, 083111 (2007).
[41]One exception is anisotropic SE emission from the clean single crystal surface in ultrahigh vacuum ($<10^{-10}$ Torr) as discussed by J. Burns [Phys. Rev. **119**, 102 (1960)].